Spectroscopy of Growing and Evaporating Water Droplets: Exploring the Variation in Equilibrium Droplet Size with Relative Humidity

Laura Mitchem,[†] Jariya Buajarern,[†] Rebecca J. Hopkins,[†,‡] Andrew D. Ward,[§] Richard J. J. Gilham,[‖,⊥] Roy L. Johnston,[‖] and Jonathan P. Reid*[,†]

School of Chemistry, University of Bristol, Bristol, BS8 1TS, United Kingdom, Lasers for Science Facility, CCLRC, Rutherford Appleton Laboratory, Chilton, Didcot, OX11 0QX, United Kingdom, and School of Chemistry, University of Birmingham, Birmingham, B15 2TT, United Kingdom

Received: February 22, 2006; In Final Form: April 25, 2006

We demonstrate that the thermodynamic properties of a single liquid aerosol droplet can be explored through the combination of a single-beam gradient force optical trap with Raman spectroscopy. A single aqueous droplet, 2−6 μm in radius, can be trapped in air indefinitely and the response of the particle to variations in relative humidity investigated. The Raman spectrum provides a unique fingerprint of droplet composition, temperature, and size. Spontaneous Raman scattering is shown to be consistent with that from a bulk phase sample, with the shape of the OH stretching band dependent on the concentration of sodium chloride in the aqueous phase and on the polarization of the scattered light. Stimulated Raman scattering at wavelengths commensurate with whispering gallery modes is demonstrated to provide a method for determining the size of the trapped droplet with nanometer precision and with a time resolution of 1 s. The polarization dependence of the stimulated scatter is consistent with the dependence observed for the spontaneous scatter from the droplet. By characterizing the spontaneous and stimulated Raman scattering from the droplet, we demonstrate that it is possible to measure the equilibrium size and composition of an aqueous droplet with variation in relative humidity. For this benchmark study we investigate the variation in equilibrium size with relative humidity for a simple binary sodium chloride/aqueous aerosol, a typical representative inorganic/aqueous aerosol that has been studied extensively in the literature. The measured equilibrium sizes are shown to be in excellent agreement with the predictions of Köhler theory. We suggest that this approach could provide an important new strategy for characterizing the thermodynamic properties and kinetics of transformation of aerosol particles.

I. Introduction

In recent years, the heterogeneity of gas−liquid surfaces has been explored in ever-increasing detail through the development of new techniques for characterizing the chemical composition and intermolecular forces acting at the surface and looking at the transfer of molecules through the interfacial region.[1−4] Nonlinear optical techniques, such as sum frequency generation, have provided invaluable insights into the orientation of surfactants at the aqueous−air surface, their impact on the hydrogen-bond network near the surface, and the extent of the electric double layer.[2,4−7] In combination with more conventional techniques, such as measurements of surface tension, neutron scattering, and ellipsometry, a plethora of techniques are now available for characterizing the structure of the gas−liquid surface.[8−11]

Characterizing the dynamics of processes occurring at the gas−liquid surface has proved more challenging. Molecular beam scattering techniques have been used to investigate the roles of inelastic scattering, trapping desorption, and desorption following reaction.[3,12,13] These studies have allowed the intermolecular interactions that govern mass transfer across the surface to be studied. Further techniques have been developed for inferring the outcome of the molecule−surface collision by characterizing the changes that occur in the gas-phase composition as molecules are adsorbed at the liquid surface. These studies include measurements in a wetted-wall flow reactor[14,15] and on a train of droplets >10 μm in radius falling under gravity.[16,17] Measurements have also been made on ensembles of aerosol particles by characterizing the evolving distributions of particle size and composition with a host of techniques including differential mobility analyzers and single-particle mass spectrometry.[18−21]

Studies of the evolving phase and composition of a single electrostatically trapped particle have yielded significant insights into the thermodynamic properties of aerosols, building on the experience of using such techniques to characterize the evaporation of a single liquid droplet of low volatility.[22,23] By combining spectroscopic techniques for characterizing the single particle with measurements of particle mass and the surrounding relative humidity (RH) of the gas phase, the hygroscopic properties of inorganic and mixed organic/inorganic aerosol particles can be examined.[24−26] Raman scattering and laser-induced fluorescence have been used to characterize the evolving droplet composition and speciation,[27] to study the state of water in a single particle,[28] and to study phase transitions such as efflorescence.[29,30]

---

* To whom correspondence should be addressed.

[†] School of Chemistry, University of Bristol, Bristol, BS8 1TS, UK

[‡] Current address: Chemical Sciences Division, Lawrence Berkeley National Laboratory, Berkeley, California 94720.

[§] Rutherford Appleton Laboratory.

[‖] University of Birmingham.

[⊥] Current address: National Physical, Laboratory, Hampton Road, Teddington, Middlesex, TW11 0LW, U.K.

10.1021/jp061135f CCC: $33.50

In this publication we describe the unique application of a single-beam gradient force optical trap (optical tweezers)[31,32] and Raman scattering in the characterization of mass transfer in the surface region of an aqueous droplet, 2−6 μm in radius. The evolving size of the trapped droplet can be probed with subnanometer precision by examining the size-dependent Raman fingerprint that is recorded.[33,34] This can permit sensitive measurements of the adsorption of only a few layers of molecules from the gas phase at the gas−liquid surface, potentially allowing direct study of uptake kinetics, measurement of mass accommodation coefficients, and study of heterogeneous reactions. In addition, the Raman fingerprint can be used to characterize the composition of the trapped droplet, not only allowing determination of the concentration of Raman-active species, but also allowing the concentration of ions and the ionic strength to be estimated.[34] Optical tweezers also allow the single particle to be trapped indefinitely, allowing accurate measurements of the thermodynamic properties of aerosols. In this publication we focus on performing such thermodynamic measurements rather than measurements of the kinetics of particle growth or evaporation. We show that measurements of equilibrium droplet size with variation in RH can be made directly and compared with Köhler theory.[35,36] We also discuss the interpretation of the Raman scattering fingerprint that is recorded from a trapped droplet.

Two competing effects determine the equilibrium size of an aqueous aerosol droplet: the surface curvature and solute effects.[35,36] The former arises from the enhanced vapor pressure of a curved surface over a flat surface, which is commonly calculated from the Kelvin equation. Although the vapor pressure tends to that of a flat surface in the limit of large droplet size, the vapor pressure remains larger than that of the flat surface even for droplets a few micrometers in diameter. Thus, at any particular droplet size supersaturation of water in the gas phase is required for an aqueous droplet to remain at an equilibrium size, i.e., the RH must be greater than 100%. If the partial pressure of water is lower than this supersaturation, the water vapor concentration at the droplet surface will be higher than that in the surrounding gas and mass transfer away from the droplet will occur, eventually leading to droplet evaporation. In competition with the surface curvature effect, an inorganic solute dissolved in the aqueous phase will lead to a lowering of the vapor pressure of the aqueous component. This reduction in vapor pressure will increase in magnitude as the droplet evaporates, and the involatile solute becomes more concentrated. Köhler theory provides a rigorous treatment of these two competing effects and can be used to estimate the droplet size at which the vapor pressure of the droplet is equal to the RH in the surrounding gas phase.[35,36] At this size there is no net mass flux to or from the droplet and an equilibrium size is achieved.

In this paper, we demonstrate that accurate measurements of droplet size allow the variation in equilibrium droplet size with RH to be measured directly for aqueous droplets doped with sodium chloride. This is chosen as a benchmark system, allowing us to rigorously test the aerosol optical tweezing technique on a binary aqueous/inorganic system containing a single salt that has been extensively studied and characterized in the literature.[36−45] Sea-salt aerosols are an important component of atmospheric models at the urban and global scales, particularly because of their impact on urban air quality and global climate.[37] The hygroscopic properties of electrolytes present in sea-salt aerosol leads to significant variations in wet particle size with relative humidity.[36,37] Thus, the size distributions of sea-salt aerosol and their optical scattering properties can vary significantly, even on a local scale.[37] The hygroscopic properties are also dependent on the organic content of the aerosol. Reduction in the deliquescence relative humidity has been reported in the presence of formic acid,[38] and suppression in the growth of sea-salt aerosol has been reported at high RH when the organic component is 10−50% of the particle mass.[39] Measurements of the optical and thermodynamic properties of sea-salt aerosol and on single salt solutions of NaCl, Na_2SO_4, $MgCl_2$, and $MgSO_4$ have been performed to investigate directly the hygroscopic properties.[40−43] It has been suggested that for dry sea-salt particles water may be present even at low RHs.[43] Further, recent studies have examined the reactions of N_2O_5 and HNO_3 on sea-salt and sodium chloride aerosols.[44,45] In this publication we take a first step toward performing such measurements on a single particle with direct in situ characterization of droplet size, composition, and phase. These measurements are performed with high temporal and spectral resolution and with the possibility of some spatial resolution. In section II we describe the experimental technique and approach, before describing the spontaneous and stimulated Raman components of the inelastically scattered light from the droplet in sections III and IV. In section V we explore the potential of this technique to characterize the equilibrium size of aqueous droplets.

II. Experimental Description

In a previous publication we described the experimental approach for trapping and manipulating aerosol droplets 2−14 μm in diameter with optical tweezers.[33] The optical trap is formed by focusing light from an argon-ion laser (514.5 nm) through a 60× oil immersion objective (NA of 1.4) with a working distance of ∼130 μm. The focused light passes through a coverslip (number 1) into an aerosol cell. A dense flow of liquid aerosol droplets, produced from an Omron NE-U07 medical nebulizer, is introduced into the cell, and a single droplet is trapped from the flow. As the flow subsides, further collisions of aerosol droplets with the trapped droplet occur and the particle grows, typically starting at a size estimated to be ∼2 μm and growing to a size that can be as large as 14 μm in diameter. Above this size, the droplet can become too large to remain trapped and is lost from the trap. Trapping efficiencies have been measured that are comparable to the trapping efficiencies reported in liquids, and laser powers as low as 1 mW are required to retain a droplet once trapped.[33]

In this publication aerosol tweezing measurements have been performed on two different instruments. The first instrument is based around a commercial Leica DM IRB microscope and has been used in our earlier work as described above.[33] The trapping beam first passes through two sets of beam expansion optics, is reflected from a holographic notch filter (HSPF-514.5, Kaiser Optical Systems), and then from a dichroic mirror onto the back aperture of the microscope objective. The cone angle of the focused light, and thus the trapping efficiency, is dependent on the positions of the beam expansion optics and the degree of overfilling of the back aperture of the objective. Backscattered light from the trapped particle passes through the holographic notch filter and is imaged onto the entrance slit of a 0.5 m spectrograph (diffraction grating blazed at 600 nm with 1200 g/mm) coupled with a CCD for recording a dispersed Raman spectrum with a spectral resolution of 0.05 nm. The polarization of the scattered light reaching the spectrograph can be selected with a polarizer in front of the entrance slit of the spectrograph. The trapped droplet is imaged using conventional brightfield microscopy with light of wavelengths longer than 700 nm passing through the dichroic mirror to record the image.

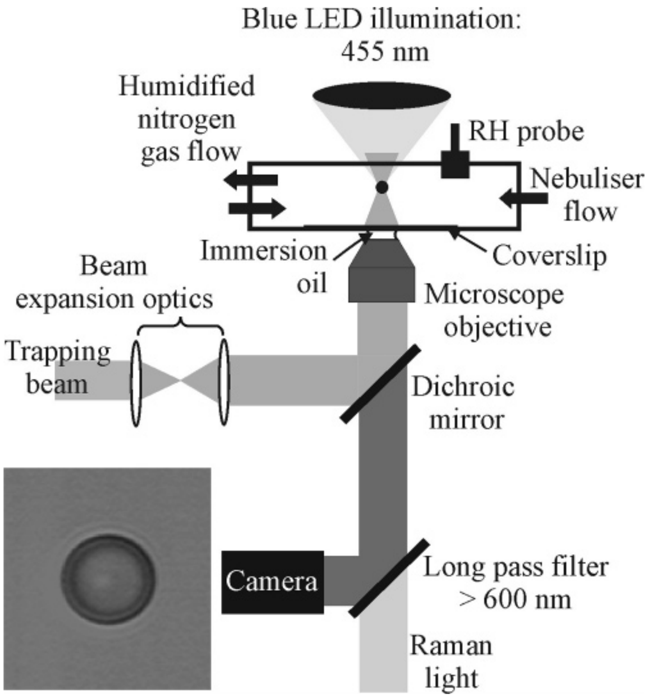

Figure 1. Experimental design. A single aerosol droplet is trapped from a nebulized flow. The relative humidity within the cell can be controlled and monitored. Illumination of the particle for imaging is achieved with a blue LED. A narrow band mirror ($\sim$99% reflective at 532 nm) is used to steer the trapping beam onto the microscope objective while allowing the blue light and Raman-scattered light around 650 nm to pass through. An image of a 5.609 μm radius water droplet is shown.

The second instrument used in this work is based around a simpler design and does not involve the use of a commercial microscope. A schematic of the instrument is shown in Figure 1. Light from a 532 nm Nd:YVO$_4$ laser (Coherent VERDI V5) is coupled into a polarization-maintaining single-mode fiber allowing the instrument to be readily aligned. The collimated output from the fiber passes through a half-wave plate and polarizing beam-splitter cube, allowing the power of the trapping beam to be controlled and also allowing orthogonal linear polarizations of the laser light to be used to trap the particle. The beam then passes through one set of beam expansion optics and reflects off a narrow band mirror (centered at 532 nm) onto the back aperture of a 100× oil immersion objective (NA of 1.25) with a working distance of $\sim$130 μm. The aerosol cell used in the first instrument is also used in this instrument. Illumination of the sample is achieved with the focused light from a blue LED (centered at 455 nm, royal blue, Luxeon III Star, Lumileds). The Raman backscattering from the trapped particle and the blue illumination light both pass through the filter to a second filter inclined at 45°. The short wavelengths in the blue are reflected to a camera for imaging and the long wavelengths imaged onto the entrance slit of a 0.5 m spectrograph (diffraction grating blazed at 500 nm, 1200 g/mm) with CCD camera, again allowing spectra to be acquired with a spectral resolution of 0.05 nm. In all of the measurements described here spectra were attained using a 1 s time integration and acquired every second, unless otherwise stated. Droplets can be trapped indefinitely with the longest measurements presented here over a time scale of 50 h.

The aerosol cell is fabricated from stainless steel with an internal diameter of $\sim$5 cm and a height of $\sim$1.5 cm. An aperture, centered on the bottom face and 2.5 cm in diameter, allows the coverslip to be mounted and held in place by a retaining ring. A sealed environment is achieved by forming an O-ring seal between the coverslip and the cell body. A top window, centered on the aperture in the bottom face and 2.5 cm in diameter, is also mounted with an O-ring seal with the illumination source passing through the window. Four ports are situated around the side wall of the cell, allowing the introduction of the aerosol flow, a humidified stream of nitrogen gas, and an outlet for the gas and aerosol flows.

Offset from the central axis of the cell a RH probe (capacitive sensor, HIH-3602-A, Honeywell Sensing and Control) continuously records the RH and temperature within the cell. A second similar RH probe is located in the incoming gas flow. The quoted accuracy on the RH measurement is ±2%. Measuring the RH on the two probes simultaneously assists in characterizing any gradients in RH that may occur within the cell. The highest RH at which measurements are made in this work is $\sim$90%. Up to this limit the quoted calibrations for RH and temperature for the two in situ probes have been compared with measurements made on two further commercially calibrated probes over a range of RHs from 25% to 92%. In addition to simultaneous ambient laboratory measurements on all four probes, measurements have been made above saturated solutions of potassium nitrate (RH = 92% at 20 °C) and potassium iodide (RH = 69% at 20 °C).[46] The two commercially calibrated probes were consistently in agreement within the stated error of each of ±2% and mostly within 1%. However, corrections were required to the calibrations of the two in situ probes with the saturated salt solutions providing convenient upper and lower bounds for calibrating the two probes for the measurements presented here. A more comprehensive discussion of this will be presented in a subsequent publication. The time constants for the response of the RH probes to fluctuations in RH are $\sim$50 s, considerably shorter than the time scales of the equilibrium size measurements discussed in section V.

The RH in the cell is controlled by varying the flow rate of dry nitrogen through a bubbler containing either pure water or a saturated salt solution, depending on the RH range required. Gas flows of up to 0.2 L/min can be used, leading to a complete refreshing of the vapor throughout the gas feed lines and cell on a time scale of $<$30 s. Short-term gradients of up to 4% can be observed between the RH probe in the input gas stream and that in the center of the cell when the RH is varied, but such gradients rapidly diminish once a constant flow of humidified nitrogen is reached. At gas flows above 0.2 L/min the trapped droplet is lost from the optical trap.

Aqueous aerosol droplets doped with sodium chloride in the concentration range 0.04−1.4 M are generated by the ultrasonic nebulizer. Doping with sodium chloride lowers the vapor pressure of the droplet to a level at which it can be trapped at RHs less than 95% within the aerosol cell. Under such conditions an aqueous droplet can be retained within the optical trap indefinitely: some measurements have been performed over time scales of 5 days. A further condition for stable trapping is that the optical trap must not heat the droplet. We discussed this crucial requirement in our earlier paper.[33] This is the primary reason for creating the optical trap from light at wavelengths between 500 and 550 nm. Within this wavelength range the complex refractive index for water is at a minimum ($<1 \times 10^{-8}$)[36] and the temperature elevation on trapping has been estimated as $\ll$1 K.[33] Further evidence for negligible heating comes from the consistent shapes of the OH Raman bands from a trapped droplet and a bulk phase measurement and from the trapping laser power independence of evaporation rates, both

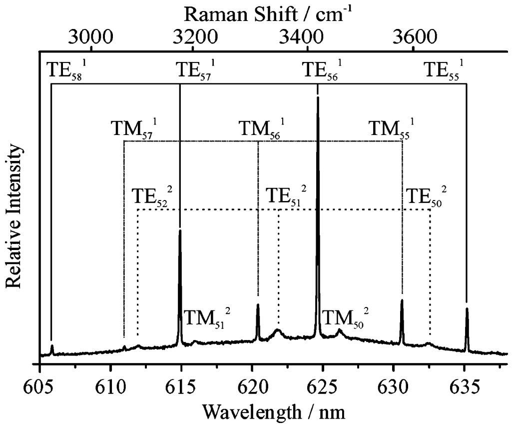

Figure 2. Example of a Raman scattering signature from a trapped water droplet, illuminated at 514.5 nm. The stimulated Raman scattering is observed at wavelengths commensurate with whispering gallery modes. The resonant modes can be assigned by comparison with Mie scattering calculations, and the droplet radius can then be calculated (5.125 μm in this case).

of which will be discussed in more detail later in this paper and in a subsequent publication.

In summary, spectral fingerprints of trapped aqueous droplets can be recorded with a time resolution of 1 s and high spectral resolution. Simultaneously, the RH and temperature of the surrounding vapor phase can be recorded along with RH and temperature gradients within the cell. Images of the trapped droplet can also be recorded, allowing direct observation of the optically trapped droplet.

III. Spontaneous Raman Scattering

A Raman scattering spectrum can be recorded from the trapped droplet, providing a unique fingerprint of droplet composition, phase, size, and refractive index.[47−52] In addition, the Raman band contours from an aqueous sample can provide a measure of temperature and ionic strength.[34,53] An example of a Raman spectrum from the OH stretching vibration of water at Stokes shifts between 2900 and 3700 cm^{-1} is shown in Figure 2 for a droplet of radius 5.125 μm. The fingerprint consists of an underlying broad spontaneous Raman band with structure from stimulated Raman scattering (SRS) superimposed. In this and the following section we explore how such a Raman fingerprint can be used to characterize all of the properties described above for a trapped droplet. We discuss the spontaneous Raman scattering in this section and the SRS in section IV.

The spontaneous Raman spectroscopy of water has been discussed in detail in the literature over many decades; see, for example refs 54−61. In this work we focus on excitation of the intramolecular OH stretching vibration, which appears at a Stokes shift of between 2900 and 3700 cm^{-1} with a maximum in intensity occurring at 3480 cm^{-1} and a strong shoulder visible at 3290 cm^{-1}. Interpretation of the shape of the broad OH stretching band has been based on ‘mixture’ or ‘continuum’ models of liquid water.[54] In the former water is assumed to be composed of a mixture of discrete species, while in the latter water is assumed to be represented by a continuum of energetic states. The shape of the band reflects the perturbation of the O−H covalent bond by the presence of intermolecular hydrogen bonds.[54]

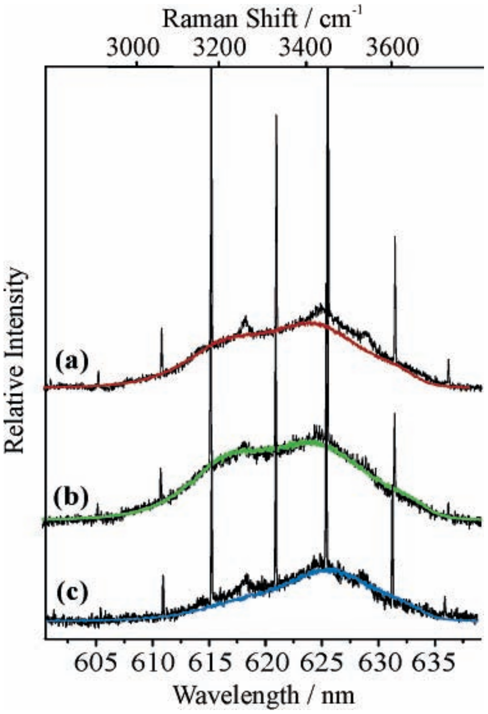

Figure 3. Dependence of the spontaneous OH stretching band shape on scattered polarization. The spectra are from (a) unpolarized collection, (b) selection of vertically polarized scatter only, and (c) selection of horizontally polarized scatter only. The bulk phase measurements of the appropriate polarization are overlaid in color, illustrating the consistency between the droplet and bulk phase measurements. Measurements were made with the trapping laser at 514.5 nm (vertically polarized) and a droplet 4.681 μm in radius.

The shape of the OH stretching band shows a systematic dependence on solute concentration in studies of aqueous solutions of inorganic solutes. This can be rationalized by changes in the hydrogen-bonding network with ionic strength.[60,62] It is common to deconvolute the band shape into as many as five different Gaussian components, with the relative weightings of each component changing with variation in ionic strength.[63] Some ions are classified as ‘structure makers’, such as F$^-$, while some as ‘structure breakers’.[62] Addition of a solute such as sodium chloride leads to disruption of the hydrogen-bonding network and reduction in the weighting of the Gaussian components representing the highly coordinated strongly hydrogen-bound water molecules.[60,62] Formation of hydrogen bonds between water and halide anions is not sufficient to compensate for the breaking of intermolecular hydrogen bonds between water molecules. Thus, with increasing salt concentration the peak maximum of the OH stretching band shifts to higher frequency and the shoulder on the low-frequency side of the Stokes band diminishes in intensity.[60,62] Similar trends in the shape of the OH band with temperature have been investigated.[55−59,61] The components centered at low Stokes shift (below 3300 cm^{-1}) decrease in weighting relative to those at higher Stokes shift with increasing temperature, reflecting the decreasing proportion of strongly hydrogen-bound water molecules of high coordination number.

A comparison between the OH stretching band shape obtained from a bulk phase measurement and that obtained from a single optically trapped droplet is shown in Figure 3a. For both the droplet and bulk phase measurements, the parallel and perpendicularly polarized components of the scattered light are convoluted in an unpolarized measurement. A slight enhancement in the parallel component over the perpendicular component arises in the spectrum due to the preferential reflectivity of the diffraction grating to the *s*-component over the *p*-

component of the scattered light. The contour of the Raman band described above with the low-frequency shoulder is clearly evident, and the droplet measurement is consistent with that observed from the bulk phase.

The polarization dependence of the scattered light is also illustrated in Figure 3b and 3c. The incident laser is vertically polarized prior to passage upward in the inverted microscope configuration. Thus, selection of the vertical polarization of the scattered light leads to collection of the parallel scattered component, while selection of the horizontal polarization leads to collection of the depolarized perpendicular component. Distinct differences are observed in the Raman band shapes between the vertical and horizontal scattered polarizations, although spectra from both polarizations are consistent for droplet and bulk phase measurements. The low-frequency shoulder has been shown to transform as a totally symmetric vibration, and this leads to an isotropic component that maintains polarization on scattering.[56,59] By contrast, the high-frequency peak has been shown to transform as an asymmetric vibration, and scattering is accompanied by a degree of depolarization; the perpendicular scattering component accompanies the parallel component.[56,59] Thus, observation of parallel polarized light leads to a spectrum that contains both isotropic and anisotropic components, while observation of the perpendicularly component leads to observation of the anisotropic component alone which arises from depolarization.[55,57]

The consistency of the bulk and droplet polarization measurements is to be anticipated based on previous experiments on electrostatically levitated droplets illuminated with a gently focused laser beam approaching the limit of plane wave illumination.[53,64] However, polarization of tightly focused laser beams, such as that used in the current study, is less well defined.[65,66] It has been reported that the state of polarization may undergo a significant change from that of the incident polarization, with the local state of polarization varying within the focal region.[65] The spatial variation in the polarization is dependent on the numerical aperture of the optical system. Despite such predicted complications in describing the polarization state of a tightly focused laser beam within a single-beam gradient force optical trap, it does appear that the backscattered Raman light retains a polarization dependence in the far field that is determined by the incident laser field prior to focusing. The degree of polarization variation that may occur within the tightly focused waist in the optical trap does not appear to scramble the scattered polarization detected in the far field.

A final comment on the consistency between the polarization measurements conducted on bulk samples and from droplets is appropriate here. The excellent agreement of the OH band shapes in bulk and droplet measurements suggests that there is little heating of the optically trapped droplet. By considering the signal-to-noise in the Raman spectrum, the intensity ratio of scattering at a Raman shift of 3440 cm^{-1} to that at 3300 cm^{-1} is 1.28 ± 0.03. On the basis of the temperature-dependent measurements of D'Arrigo, an uncertainty in temperature of ± 3 °C can be estimated from the uncertainty in the intensity ratio.[58] That is, within the signal-to-noise of our measurements the temperature of the droplet could differ by up to 3 °C from that of the bulk phase sample. Although this only places an upper limit on the degree of heating that could be occurring, the experimental data remain consistent with our earlier predictions that only a very minor temperature increase above ambient of <1 °C is anticipated.[33]

IV. Stimulated Raman Scattering

It is has been widely reported that the Raman spectrum from a droplet with a size within the Mie regime shows distinct features not observed in a bulk phase sample.[23,34,49,51,67] In addition to the underlying spontaneous Raman scattering, SRS is also observed at discrete wavelengths and a structured fingerprint is observed.[52] In the spectrum of Figure 2 the maximum intensity of the SRS is approximately a factor of 15 more intense than the spontaneous Raman scattering band. Amplification of the Raman-scattered light occurs only at the distinct wavelengths that are commensurate with whispering gallery modes (WGMs).[67] WGMs are also commonly referred to as morphology-dependent resonances or cavity resonances. In this section we describe the SRS component of the Raman fingerprint from the trapped droplet.

At wavelengths commensurate with WGMs, the Raman light can become trapped by total internal reflection within the droplet; the droplet behaves as a low-loss optical cavity.[67,68] The simultaneous presence of the illuminating excitation wavelength and the Raman-scattered wavelengths within the droplet leads to SRS, which occurs at a lower threshold in laser intensity than is needed in the bulk phase. The quality factors of the resonant modes can be in excess of 10^6, leading to WGM excitation lifetimes on the order of nanoseconds.[67,68]

Mie scattering calculations can be performed to determine the wavelengths at which WGMs are formed. Comparing the observed WGM wavelengths from a Raman or fluorescence fingerprint, such as that in Figure 2, with calculated wavelengths can enable the droplet size to be determined with high precision.[51,69] Lin et al. demonstrated that the size can be determined with a precision equivalent to 1 nm for a droplet 5 μm in radius.[69] Such a degree of precision requires an accurate knowledge of the refractive index of the droplet. Indeed, the dispersion in the refractive index can be determined, leading to an assessment of temperature gradients within a droplet.[69]

We discussed in a previous publication the algorithm by which we determine the size of aqueous droplets and errors associated with such a determination.[70] For the work presented here, we used the formulation of the refractive index described by Millard et al. for seawater.[71] Although seawater contains trace components other than sodium chloride and water, the wavelength, temperature, and salinity parametrization of the algorithm provides an extremely convenient functional form for determining the refractive index of the droplet. In addition, it reproduces the reported refractive indices of sodium chloride solution at 589 nm with an accuracy of better than 0.05% at the concentrations of sodium chloride used in this work.[46]

Comparison of the calculated and measured Raman fingerprints and refinement of the fit allows the droplet size to be calculated with a precision estimated to be of the order of ± 1 nm, with the accuracy of the fit determined by the accuracy of the refractive index data.[70] The WGMs appearing in the fingerprint are assigned a mode number, n, which defines the number of wavelengths forming the standing wave around the droplet circumference, and a mode order, l, which defines the number of maxima in the radial distribution of the mode intensity.[67,69] For the droplet sizes investigated here only first- and second-order modes can contribute to the SRS signal.[69,72] Finally, the mode can be assigned as being a transverse electric (TE) mode with no radial dependence in the electric field or as a transverse magnetic (TM) mode with no radial dependence in the magnetic field. A full assignment of the modes is shown in Figure 2, where the polarization is specified and the mode number is indicated by the subscript and the order by the

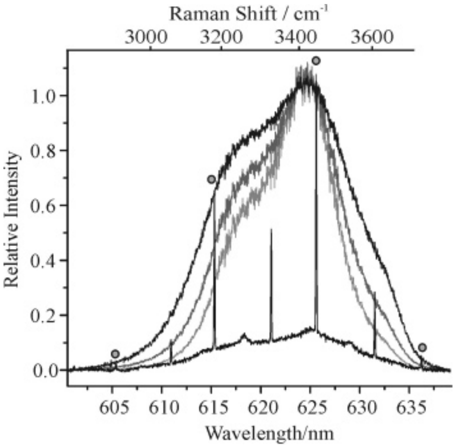

Figure 4. Demonstration of the consistency between the spontaneous and stimulated Raman band shapes. The bulk phase spontaneous Raman band is scaled according to eq 1 to give the black, dark gray, and gray curves overlaid with the droplet Raman fingerprint with gains of 0, 1, and 2, respectively. The SRS for progression of modes indicated by the filled circles is consistent with a bulk phase measurement with a gain of zero. Measurements were made with the trapping laser at 514.5 nm (vertically polarized, unpolarized collection) and a droplet 4.681 μm in radius.

superscript. The droplet is calculated to have a radius of 5.125 μm, and all droplet sizes should be assumed to be quoted with a precision of ±1 nm.

The nonlinear behavior of the SRS signal indicates that the SRS band shape is related to the spontaneous band by an exponential scaling.[34] In its simplest form, the stimulated Raman intensity, $I_{\mathrm{SRS}}(\lambda)$, can be written as

$$I_{\mathrm{SRS}}(\lambda) = I_0(\lambda)\exp[G(g(\lambda) - 1)] \tag{1}$$

where I_0 is the intensity of the spontaneous scatter at wavelength λ, G is a gain factor reflecting the degree of amplification of the Raman light, and $g(\lambda)$ is a line shape function describing the shape of the spontaneous band. The predicted variation in the SRS line shape with gain factor is shown in Figure 4 and compared with a spectrum from a droplet 4.681 μm in radius. Both the bulk phase measurement for the gain scaling and the droplet measurement are recorded with unpolarized collection of scattered light. It is clear that progressions of the same mode order and polarization display a trend in intensity that is consistent with the spontaneous scattering band of the same polarization. Indeed, in this case it is clear that the gain factor is very low, $\sim$0; the SRS is just above threshold and only weakly enhanced over the spontaneous scattering intensity. Similar behavior is observed for all of the measurements presented in this publication. The change in the expected SRS envelope is shown for higher gains of 1 and 2. It should be noted that the gain is considerably less than the much higher gains of 10−15 that are observed in SRS from droplets illuminated with the much higher peak irradiances obtained from a pulsed laser source.[34]

For the same droplet characterized in the spectra of Figures 3 and 4, the intensity envelope of the SRS is consistent with the bulk phase spectrum of the appropriate polarization, as illustrated in Figure 5. This indicates that the SRS signal reflects the polarization dependence of the spontaneous line shape even when a specific polarization is monitored, again suggesting that polarization-dependent measurements can be made even with optically trapped droplets from a high NA objective. Again, although the SRS surpasses threshold, the gain factor is $\ll$1. The dominant progression of modes can be assigned to a progression of first-order TE modes when the unpolarized and vertically polarized spectra are recorded (Figure 5a and 5b, respectively). However, on recording the horizontal polarization of the scattered light, the corresponding progression of first-order TM modes is dominant (Figures 5c).

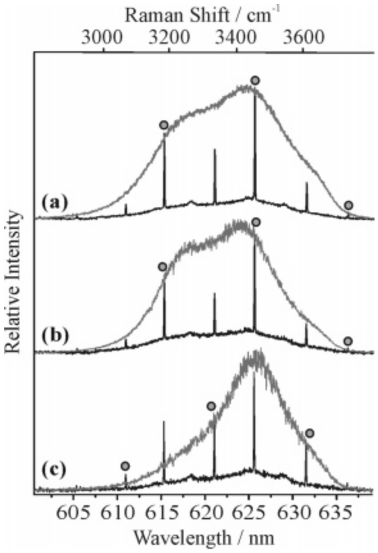

Figure 5. Polarization dependence of the SRS reflects the polarization dependence of the spontaneous scattering intensity. Unpolarized, vertically polarized, and horizontally polarized scattering components are shown in a, b, and c, respectively, and comparison between the droplet and bulk phase measurements is good. Measurements were made with the trapping laser at 514.5 nm (vertically polarized, unpolarized collection) and a droplet 4.681 μm in radius.

The Raman spectra discussed so far have all been accumulated from the Raman signal integrated over the entire CCD detector with no particular spatial selection of signal on the CCD. A degree of spatial resolution in the light scattering can be achieved by resolving the Raman image on the CCD detector, examining the spectral dependence on different rows of the 256-row detector. A similar approach has been used by Chan and co-workers to spatially profile the concentration of NO_3^- within an aqueous droplet.[73] This previous work was for considerably larger droplets than those discussed here with a typical diameter of around 30 μm.[74] Care must be taken in interpreting the spatially resolved signal from tweezed droplets collected through a high NA objective. Signal variability arises from a convolution of the incident light field acting as a source function, the scattered field, which will show strong variations with scattering angle, and the variation in collection efficiency with scattering angle.[49] Although a fuller investigation of these factors will be discussed in later work, for this work it is instructive to examine the variation in Raman signature with position on the CCD detector.

A Raman image is illustrated in Figure 6. The spontaneous Raman intensity is at a maximum from the center of the droplet on the axis of the trapping beam, and this appears in the central rows of the Raman image. In this region the spontaneous signal dominates any signal from stimulated scatter, leading to a signal that could allow the unambiguous quantification of trace species without complication from WGMs. In addition, the spontaneous band can be rigorously compared with bulk phase measurements free from interference from WGMs. In contrast, signal which appears to come from the edge region of the droplet is dominated by SRS, and the WGMs can allow the accurate determination of droplet size. Spatially resolving the signal on the CCD detector can thus allow discrimination in favor of detecting spontaneous or stimulated signal.

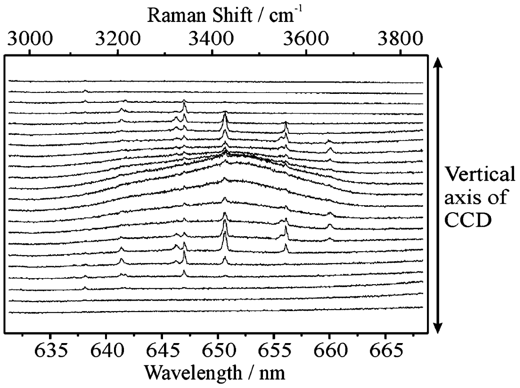

Figure 6. Spatially resolved Raman image from a droplet 5.609 μm in radius. Spontaneous scatter is observed to dominate in the center of the image, arising principally from the center of the droplet where the laser intensity is at its largest. The stimulated scatter dominates at the edges of the image. Measurements were made with the trapping laser at 532 nm (vertically polarized, unpolarized collection).

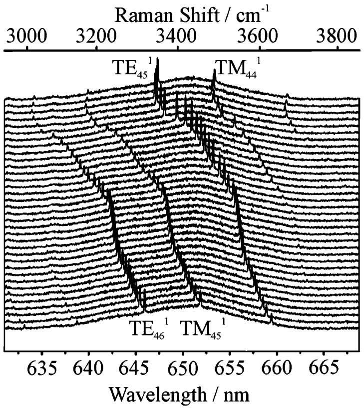

Figure 7. Small changes in droplet size are reflected by changes in the wavelengths of stimulated Raman scattering with time. The initial droplet size is 3.986 μm, and the final size is 3.913 μm. This size change occurs over a period of ~30 min with each time frame recorded from a 5 s integration. Only 1 in every 10 frames is shown for clarity. Measurements were made with the trapping laser at 532 nm (vertically polarized, unpolarized collection).

V. Thermodynamic Measurements of Equilibrium Droplet Size

The spectroscopic tools described above are now applied to the characterization of droplet size and composition and the dependence of equilibrium droplet size on RH and particle composition. To assess our ability to measure a Köhler curve directly with this technique, we performed measurements of equilibrium droplet size with varying RH in the range from ~80% to 92%, starting with droplets with initial sodium chloride concentrations of between 0.04 and 1.28 M. For a droplet initially trapped with a wet particle radius of 5 μm, typical in this work, these salt concentrations correspond to a range in the dry particle radius of 500 nm to 1.6 μm, assuming a density for sodium chloride of 2.165 g/cm^3.[46]

A typical time history in the evolution of a trapped droplet Raman fingerprint is shown in Figure 7. Once trapped, the particle responds to variations in the RH of the surrounding vapor, tending eventually toward an equilibrium size that can be estimated by Köhler theory. Each spectrum in Figure 7 corresponds to an integration time of 5 s, and only 1 spectrum in every 10 is shown. Thus, this evolution in droplet size occurs over a time frame of ~30 min. The initial size of the particle is 3.986 ± 0.001 μm, and the final size is 3.913 ± 0.001 μm, showing that over this time frame the droplet decreases in size by only 73 nm. The assignment of WGMs appearing in the spectrum is reported in the figure. As the droplet evaporates, the circumference of the droplet decreases and the path length of a WGM with a particular mode number decreases. Thus, the wavelength shifts to the blue. For a growing droplet, the WGM are observed to shift toward the red.

To compare measurements of equilibrium droplet size with Köhler theory, the composition of the droplet must be known, allowing the dry particle size (or solute concentration) to be estimated.[35] Although a solution of a particular salt concentration is nebulized, it is not certain that the salt concentration of a droplet once trapped will be equivalent to this starting concentration in the nebulizer. Mass transfer and coagulation in the aerosol stream with partial or full equilibration to the rapidly varying local RH could scramble the mass loading of salt in each trapped aerosol droplet. Once trapping has occurred, a droplet may undergo further collisions with droplets in the nebulized stream before the flow of aerosol subsides, leading to the dosing of extra solute mass into the trapped droplet. An approach for the in situ characterization of the solute concentration is required. With solutes such as nitrate and sulfate, this may be achieved by Raman spectroscopy; with sodium chloride, direct quantification of the salt loading in the trapped droplet by Raman spectroscopy is not possible.

In section III we described in detail the shape of the OH band contour, the dependence on polarization and temperature, and the impact of ionic solutes through their influence on the hydrogen-bonding network. It has been widely reported that disruption of the hydrogen-bonding network through inclusion of ions such as chloride leads to a weakening in intensity of the low Stokes frequency shoulder.[60,62] A significant change in the intensity of the shoulder has been observed at concentrations between 0 and 1 M, corresponding to the expected concentration range of trapped aqueous droplets in this work. Thus, by integrating the Raman signal from the center of the Raman image, a comparison of the OH band contour from the droplet with bulk phase standards could allow the concentration of sodium chloride to be assessed. The discussion of polarization measurements in section III confirms that a direct comparison can be made.

Comparison of the spontaneous Raman scattering from droplets generated from bulk solutions of 0.04, 0.34, and 1.28 M is shown in Figure 8a−c, along with corresponding bulk phase measurements. Excellent conformity between the droplet and bulk phase measurements is observed for the two lower concentrations, although some deviation is observed between the droplet and bulk measurements for the higher concentration. Furthermore, a comparison of the OH band contours from droplets generated from the three different concentrations clearly illustrates the decline in the intensity of the shoulder with increasing salt concentration, Figure 8d. This demonstrates that examining the spontaneous band shape could allow the concentration of the solute to be determined. We shall return to this later.

A complete time history of the evolving radius of a trapped droplet over a time scale of 50 h is shown in Figure 9a. Raman spectra were acquired at 5 s intervals, along with measurements of the RH within the cell. The variation in RH is shown for comparison. The oscillations in RH that occur as a result of the laboratory air conditioning system are clearly visible in the oscillations in particle size, as illustrated in Figure 9b. These oscillations correspond to a change in RH of ~0.2% and a change in radius of ~30 nm, a size change that is clearly discernible in our measurements. Indeed, the droplet could be

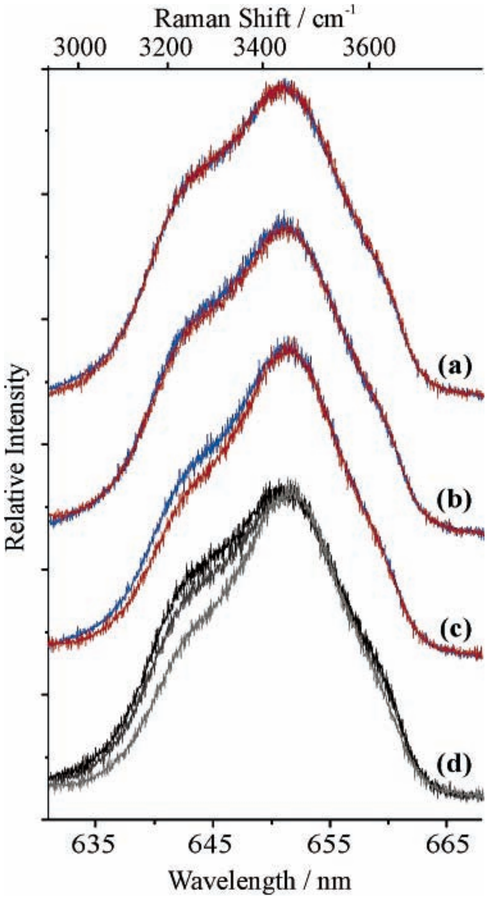

Figure 8. Variation in the OH band shape with sodium chloride concentration. The blue spectra are from bulk phase measurements on solutions of 0.04, 0.34, and 1.28 M (a, b, and c, respectively). Measurements on trapped droplets, produced by nebulizing each of the solutions in turn and selecting only the spontaneous Raman scattering from the center of the Raman image, are overlaid for comparison in red. The three droplet measurements are shown in d for comparison, with the 0.04 M spectrum showing the most intense shoulder and the 1.28 M the least intense. Measurements were made with the trapping laser at 532 nm (vertically polarized, unpolarized collection).

considered to act as a more accurate probe of RH than the RH probe used in the cell. It should be remembered that the accuracy of the RH determination by the two probes is ±2%.

A comparison of the equilibrium size measurements with Köhler theory is shown in Figure 10. The calculations from Köhler theory have been described in previous publications, and the details will not be reported here.[35,75,76] However, it is important to note that the theory is well established for inorganic/aqueous droplets. The treatment used here includes the deviation from ideal solution behavior through an activity coefficient that is not unity, and it also explicitly includes all ionic interactions and multicomponent surface tensions.[75,76] The earliest time measurements within the first hour of trapping are poorly correlated with the calculations from Köhler theory. During this period the cell may contain surface water deposited from the initial aerosol burst, and it takes sometime for the cell to equilibrate due to evaporation of surface water. During this time gradients in RH within the cell lead to a poor correspondence between the measured RH (measured to be greater than 90%) and the RH in the locality of the trapped droplet. It should be noted that the early time data is not shown in Figure 9: all of the data recorded in Figure 9 corresponds to the equilibrium size measurements shown in black in Figure 10.

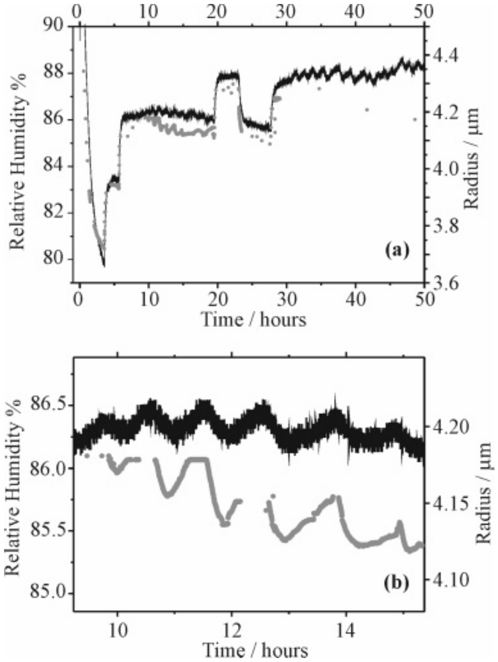

Figure 9. (a) By assigning the SRS fingerprints and determining the size with nanometer precision, the change in equilibrium droplet size (gray circles, right axis) with change in relative humidity (black line, left axis) can be measured. (b) Expanded view of the variation between 10 and 15 h. Measurements were made with the trapping laser at 532 nm.

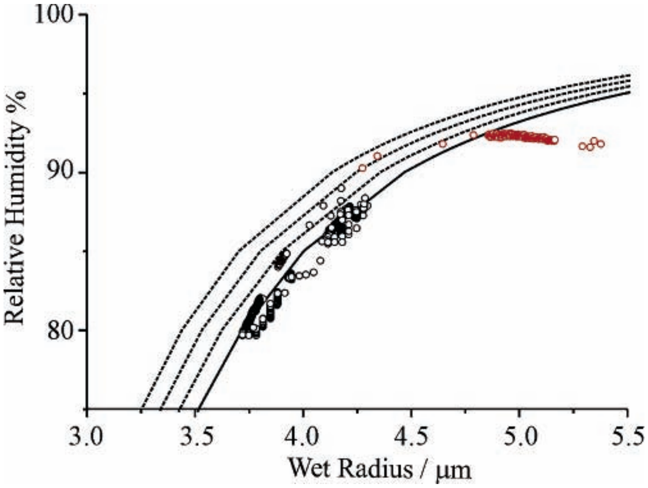

Figure 10. Comparison of the measured equilibrium sizes with change in relative humidity with predictions from Köhler theory for particles of varying dry diameter. The four Köhler curves shown are for dry particles with radii of 1714, 1761, 1807, and 1853 nm from leftmost to rightmost curves, respectively. At early times, RH gradients are observed in the cell which lead to measurements that do not compare well with Köhler theory (shown by red circles). At longer times, after ~1 h, agreement is excellent between the measurements and Köhler predictions (black circles).

After this initial period of equilibration of approximately 1 h the equilibrium droplet sizes show a good correspondence with the Köhler predictions for a dry particle of radius 1853 nm. If the original droplet is assumed to have the same concentration as the nebulized solution, 1.28 M, the initial droplet of 5.5 μm radius would contain a mass loading equivalent to a dry particle size of 1.8 μm, very comparable to the dry particle mass estimated from Köhler theory. This is considered excellent agreement based on the accuracy of the RH measurements of ±2%.

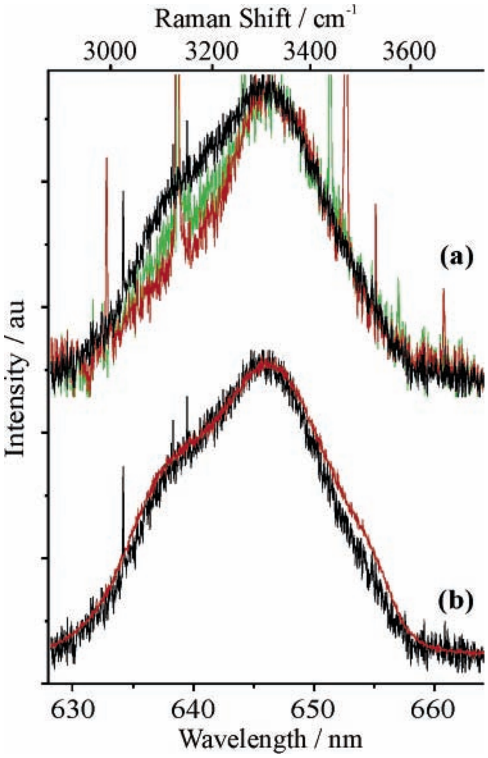

Figure 11. (a) Comparison of the spontaneous Raman band shape for the droplet studied in Figures 9 and 10 when at a radius of 5.5, 4.1, and 3.8 μm (black, green and red, respectively). Increasing concentration of the sodium chloride is evident with decreasing droplet size. (b) Comparison of the spontaneous Raman band shape for the droplet at a radius of 5.5 μm with the bulk phase measurement at a concentration of 0.34 M. Measurements were made with the trapping laser at 532 nm (vertically polarized, unpolarized collection).

Variations in the OH band shape with droplet size for the droplet studied in Figures 9 and 10 are shown in Figure 11a. Spectra when the droplet size is 5.5 (when first trapped), 4.1, and 3.8 μm are shown to allow comparison. The concentration of the sodium chloride is clearly shown to rise as the droplet becomes smaller, with the shoulder diminishing in intensity with decreasing size. Although the presence of cavity resonances complicates the analysis, the comparison between the spectra recorded from the droplet when it is first trapped with a radius of 5.5 μm and a 0.34 M bulk solution is better than the comparison with a 1.28 M bulk solution. A droplet with a concentration of 0.34 M would contain 13.9 pg of sodium chloride, corresponding to a dry particle of radius 1.2 μm, a considerable underestimation of the dry particle size when compared with the concentration of nebulized solution and predictions from Köhler theory of 1.8 μm discussed above. However, the signal-to-noise ratio in these spectra and the lack of a quantitative calibration of ion concentration at intermediate concentrations limits the extent of the conclusions that can be drawn from the shape of the OH band.

These data clearly show that with the high precision in size determination available from SRS measurements and the ability to trap a single aqueous droplet for long periods of time, direct measurements can be made of the Köhler curves by measuring the equilibrium wet droplet size for inorganic−aqueous droplets.

VI. Conclusions

We demonstrated that a single aqueous aerosol droplet can be trapped with optical tweezers for an indefinite period. In addition, we showed that spectroscopic characterization of the droplet can lead to determination of droplet size with nanometer precision and that the concentration of ionic solutes in the droplet can be investigated from the shape of the OH Raman stretching band. This is possible because the spectroscopic signature from the droplet can be directly compared with bulk phase measurements on solutions of known concentration, with the polarization dependence of the spontaneous and stimulated Raman bands conforming to that observed in measurements in the bulk aqueous phase. In applying the technique in measurements of equilibrium droplet size with variation in RH, excellent agreement between the experimental determination and Köhler prediction is achieved. The data are consistent assuming that the sodium chloride concentration in the droplet when initially trapped is equal to the concentration of sodium chloride in the nebulized solution.

It is anticipated that the approach described here can be used to characterize the thermodynamic properties of aerosols and test Köhler theory directly. Of particular importance for atmospheric chemistry will be the potential to compare the measured and calculated properties of multicomponent aqueous/inorganic/organic droplets and the properties of multiphase aerosol in which the separation of immiscible organic and aqueous phases could be strongly dependent on RH.[75,76] Multiple optical traps can also be established, allowing two or more droplets to be trapped simultaneously.[33] In current work we are trapping a sodium chloride/aqueous droplet in one optical trap as a control droplet, providing an accurate method for determining the RH within the trapping region. This then allows the equilibrium behavior of a second droplet of different composition to be accurately investigated.

Not only can aerosol optical tweezers allow us to study the equilibrium behavior of droplets, but the technique can also permit direct measurements of mass transfer rates with studies of the kinetics of particle growth and measurements of evolving size and composition being possible. Further, the simultaneous trapping of multiple particles in parallel optical traps can allow measurements to be made on aerosol arrays. This could allow us to examine competitive growth rates, allowing relative rates to be correlated to relative mass accommodation coefficients for a trace species on two different aerosol surfaces. The near-surface origin of the stimulated Raman scattering could yield important information on the existence of concentration gradients within the droplet in organic coated/doped droplets and on the mixing state of different aerosol components. Finally, through the controlled coagulation of two aerosol particles in two optical traps, the fundamental factors governing interparticle interactions, mixing state, and aerosol coagulation can be studied directly for the first time.[33]

Acknowledgment. We acknowledge the EPSRC for financial support for this work and supporting L.M.. We also acknowledge Dr. G. McFiggans and Dr. D. Topping for performing the Köhler calculations and discussing this work. R.J.H. acknowledges NERC for financial support. The award of CCLRC facility time at the LSF (CM1C1/05) is also gratefully acknowledged. Mr. Jason Butler is also acknowledged for his contribution at the final stages of the preparation of this manuscript.

References and Notes

(1) Nathanson, G. M. *Annu. Rev. Phys. Chem.* **2004**, *55*, 231.

(2) Mucha, M.; Frigato, T.; Levering, L. M.; Allen, H. C.; Tobias, D. J.; Dang, L. X.; Jungwirth, P. *J. Phys. Chem. B* **2005**, *109*, 7617.

(3) Nathanson, G. M.; Davidovits, P.; Worsnop, D. R.; Kolb, C. E. *J. Phys. Chem.* **1996**, *100*, 13007.

(4) Raymond, E.; Tarbuck, T.; Brown, M.; Richmond, G. *J. Phys. Chem. B* **2003**, *107*, 546.
(5) Shultz, M. J.; Baldelli, S.; Schnitzer, C.; Simonelli, D. *J. Phys. Chem. B* **2002**, *106*, 5313.
(6) Gragson, D. E.; Richmond, G. L. *J. Phys. Chem. B* **1998**, *102*, 3847.
(7) Liu, D. F.; Ma, G.; Levering, L. M.; Allen, H. C. *J. Phys. Chem. B* **2004**, *108*, 2252.
(8) Demou, E.; Donaldson, D. J. *J. Phys. Chem. A* **2002**, *106*, 982.
(9) Penfold, J.; Tucker, I.; Thomas, R. K.; Zhang, J. *Langmuir* **2005**, *21*, 10061.
(10) Wilkinson, K. M.; Lei, Q. F.; Bain, C. D. *Soft Matter* **2006**, *2*, 66.
(11) Zhang, J.; Thomas, R. K.; Penfold, J. *Soft Matter* **2005**, *1*, 310.
(12) Kohler, S. P. K.; Allan, M.; Kelso, H.; Henderson, D. A.; McKendrick, K. G. *J. Chem. Phys.* **2005**, *122*.
(13) Lawrence, J. R.; Glass, S. V.; Nathanson, G. M. *J. Phys. Chem. A* **2005**, *109*, 7449.
(14) Leyssens, G.; Louis, F.; Sawerysyn, J. P. *J. Phys. Chem. A* **2005**, *109*, 1864.
(15) Esteve, W.; Noziere, B. *J. Phys. Chem. A* **2005**, *109*, 10920.
(16) Gershenzon, M.; Davidovits, P.; Williams, L. R.; Shi, Q. A.; Jayne, J. T.; Kolb, C. E.; Worsnop, D. R. *J. Phys. Chem. A* **2004**, *108*, 1567.
(17) Zhang, H. Z.; Davidovits, P.; Williams, L. R.; Kolb, C. E.; Worsnop, D. R. *J. Phys. Chem. A* **2005**, *109*, 3941.
(18) Katrib, Y.; Biskos, G.; Buseck, P. R.; Davidovits, P.; Jayne, J. T.; Mochida, M.; Wise, M. E.; Worsnop, D. R.; Martin, S. T. *J. Phys. Chem. A* **2005**, *109*, 10910.
(19) Tolocka, M. P.; Saul, T. D.; Johnston, M. V. *J. Phys. Chem. A* **2004**, *108*, 2659.
(20) Hallquist, M.; Stewart, D. J.; Baker, J.; Cox, R. A. *J. Phys. Chem. A* **2000**, *104*, 3984.
(21) Stewart, D. J.; Griffiths, P. T.; Cox, R. A. *Atmos. Chem. Phys.* **2004**, *4*, 1381.
(22) Davis, E. J. *Aerosol Sci. Technol.* **1997**, *26*, 212.
(23) Davis, E. J.; Schweiger, G. *The Airborne Microparticle*; Springer: New York, 2002.
(24) Peng, C.; Chan, M. N.; Chan, C. K. *Environ. Sci. Technol.* **2001**, *35*, 4495.
(25) Choi, M. Y.; Chan, C. K. *Environ. Sci. Technol.* **2002**, *36*, 2422.
(26) Choi, M. Y.; Chan, C. K. *J. Phys. Chem. A* **2002**, *106*, 4566.
(27) Zhang, Y. H.; Chan, C. K. *J. Phys. Chem. A* **2002**, *106*, 285.
(28) Choi, M. Y.; Chan, C. K.; Zhang, Y. H. *J. Phys. Chem. A* **2004**, *108*, 1133.
(29) Colberg, C. A.; Krieger, U. K.; Peter, T. *J. Phys. Chem. A* **2004**, *108*, 2700.
(30) Choi, M. Y.; Chan, C. K. *J. Phys. Chem. A* **2005**, *109*, 1042.
(31) Molloy, J. E.; Padgett, M. J. *Contemp. Phys.* **2002**, *43*, 241.
(32) Ashkin, A.; Dziedzic, J. M.; Bjorkholm, J. E.; Chu, S. *Opt. Lett.* **1986**, *11*, 288.
(33) Hopkins, R. J.; Mitchem, L.; Ward, A. D.; Reid, J. P. *Phys. Chem. Chem. Phys.* **2004**, *6*, 4924.
(34) Symes, R.; Sayer, R. M.; Reid, J. P. *Phys. Chem. Chem. Phys.* **2004**, *6*, 474.
(35) McFiggans et al. *Atmos. Chem. Phys. Discuss.* **2005**, *5*, 8507.
(36) Seinfeld, J. H.; Pandis, S. N. *Atmospheric Chemistry and Physics: From Air Pollution to Climate Change*; John Wiley & Sons: New York, 1998.
(37) Zhang, K. M.; Knipping, E. M.; Wexler, A. S.; Bhave, P. V.; Tonnesen, G. S. *Atmos. Environ.* **2005**, *39*, 3373.
(38) Xu, Q.; DeWitte, M.; Sloan, J. J. *Atmos. Environ.* **2003**, *37*, 911.
(39) Randles, C. A.; Russell, L. M.; Ramaswamy, V. *Geophys. Res. Lett.* **2004**, *31*.
(40) Steiner, B.; Berge, B.; Gausmann, R.; Rohmann, J.; Ruhl, E. *Appl. Opt.* **1999**, *38*, 1523.
(41) Weis, D. D.; Ewing, G. E. *J. Geophys. Res. Atmos.* **1999**, *104*, 21275.
(42) Tang, I. N.; Munkelwitz, H. R.; Wang, N. *J. Colloid Interface Sci.* **1986**, *114*, 409.
(43) Tang, I. N.; Tridico, A. C.; Fung, K. H. *J. Geophys. Res. Atmos.* **1997**, *102*, 23269.
(44) Thornton, J. A.; Abbatt, J. P. D. *J. Phys. Chem. A* **2005**, *109*, 10004.
(45) Haddrell, A. E.; Feng, X.; Nassar, R.; Bogan, M. J.; Agnes, G. R. *J. Aerosol Sci.* **2005**, *36*, 521.
(46) *Handbook of Chemistry and Physics*, 84th ed.; CRC Press LLC: Boca Raton, FL, 2003−2004.
(47) Tang, I. N.; Fung, K. H. *J. Chem. Phys.* **1997**, *106*, 1653.
(48) Fung, K. H.; Imre, D. G.; Tang, I. N. *J. Aerosol Sci.* **1994**, *25*, 479.
(49) Schweiger, G. *J. Aerosol Sci.* **1990**, *21*, 483.
(50) Musick, J.; Popp, J.; Kiefer, W. *J. Raman Spectrosc.* **2000**, *31*, 217.
(51) Popp, J.; Lankers, M.; Trunk, M.; Hartmann, I.; Urlaub, E.; Kiefer, W. *Appl. Spectrosc.* **1998**, *52*, 284.
(52) Thurn, R.; Kiefer, W. *Appl. Opt.* **1985**, *24*, 1515.
(53) Vehring, R.; Schweiger, G. *Appl. Spectrosc.* **1992**, *46*, 25.
(54) Walrafen, G. E. Raman and Infrared Spectral Investigations of Water Structure. In *Water: A Comprehensive Treatise*; Franks, F., Ed.; Plenum: New York, 1972; Vol. 1, p 151.
(55) Scherer, J. R.; Go, M. K.; Kint, S. *J. Phys. Chem.* **1974**, *78*, 1304.
(56) Terpstra, P.; Combes, D.; Zwick, A. *J. Chem. Phys.* **1990**, *92*, 65.
(57) Hare, D. E.; Sorensen, C. M. *J. Chem. Phys.* **1990**, *93*, 25.
(58) Darrigo, G.; Maisano, G.; Mallamace, F.; Migliardo, P.; Wanderlingh, F. *J. Chem. Phys.* **1981**, *75*, 4264.
(59) Cunningham, K.; Lyons, P. A. *J. Chem. Phys.* **1973**, *59*, 2132.
(60) Li, R. H.; Jiang, Z. P.; Chen, F. G.; Yang, H. W.; Guan, Y. T. *J. Mol. Struct.* **2004**, *707*, 83.
(61) Walrafen, G. E.; Fisher, M. R.; Hokmabadi, M. S.; Yang, W. H. *J. Chem. Phys.* **1986**, *85*, 6970.
(62) Lilley, T. H. Raman Spectroscopy of Aqueous Electrolyte Solutions. In *Water: A Comprehensive Treatise*; Franks, F., Ed.; Plenum: New York, 1973; Vol. 3, p 265.
(63) Carey, D. M.; Korenowski, G. M. *J. Chem. Phys.* **1998**, *108*, 2669.
(64) Fung, K. H.; Tang, I. N. *Appl. Spectrosc.* **1992**, *46*, 1189.
(65) Lekner, J. *J. Opt. A* **2003**, *5*, 6.
(66) Lindfors, K.; Setala, T.; Kaivola, M.; Friberg, A. T. *J. Opt. Soc. Am. A* **2005**, *22*, 561.
(67) Hill, S. C.; Benner, R. E. Morphology-Dependent Resonances. In *Optical Effects Associated with Small Particles*; Barber, P. W., Chang, R. K., Eds.; World Scientific: Singapore, 1988; Vol. 1, p 3.
(68) Campillo, A. J.; Eversole, J. D.; Lin, H. B. In *Optical Processes in Microcavities*; Chang, R. K., Campillo, A. J., Eds.; World Scientific: Singapore, 1996; Chapter 5.
(69) Eversole, J. D.; Lin, H. B.; Huston, A. L.; Campillo, A. J.; Leung, P. T.; Liu, S. Y.; Young, K. *J. Opt. Soc. Am. B* **1993**, *10*, 1955.
(70) Sayer, R. M.; Gatherer, R. D. B.; Gilham, R.; Reid, J. P. *Phys. Chem. Chem. Phys.* **2003**, *5*, 3732.
(71) Millard, R. C.; Seaver, G. *Deep-Sea Res. a* **1990**, *37*, 1909.
(72) Biswas, A.; Latifi, H.; Armstrong, R. L.; Pinnick, R. G. *Phys. Rev. A* **1989**, *40*, 7413.
(73) Zhang, Y. H.; Choi, M. Y.; Chan, C. K. *J. Phys. Chem. A* **2004**, *108*, 1712.
(74) Zhang, Y. H.; Chan, C. K. *J. Phys. Chem. A* **2000**, *104*, 9191.
(75) Topping, D. O.; McFiggans, G. B.; Coe, H. *Atmos. Chem. Phys.* **2005**, *5*, 1205.
(76) Topping, D. O.; McFiggans, G. B.; Coe, H. *Atmos. Chem. Phys.* **2005**, *5*, 1223.